The Thesis Committee for Sridharan Thirumalai Vasu
Certifies that this is the approved version of the following Thesis:

Design and Computational Optimization of a Flexure-based XY Nano-positioning Stage

APPROVED BY
SUPERVISING COMMITTEE:

Michael A. Cullinan, Supervisor

Richard H. Crawford

Design and Computational Optimization of a Flexure-based XY Nano-positioning Stage

by

Sridharan Thirumalai Vasu

Thesis

Presented to the Faculty of the Graduate School of

The University of Texas at Austin

in Partial Fulfillment

of the Requirements

for the Degree of

Master of Science in Engineering

The University of Texas at Austin

May 2019

Dedication

To my parents, friends and family for their support and encouragement.

Acknowledgements

I would like to express my heartfelt gratitude to my advisor, Dr. Michael Cullinan, for providing the opportunity to work on this project. I appreciate his constant support, advice, and encouragement to pursue this research with a lot of freedom. I am grateful to Dr. Nilabh Roy for his help in conceptualizing the project and his guidance in overcoming obstacles every step of the way. I acknowledge my lab-mates Martin Ward, Dipankar Behera, Liam Connolly, David Cayll, Georgina Dibua and Dr. Tsung-Fu Yao for their invaluable support, advice and friendship during my time here. I would also like to thank my committee reader Dr. Richard Crawford for his valuable feedback. Finally, my parents, friends and family have been my cornerstone, and I would like to thank them from the bottom of my heart for keeping me motivated towards achieving my goals.

Abstract

Design and Computational Optimization of a Flexure-based XY Nano-positioning Stage

Sridharan Thirumalai Vasu, M.S.E

The University of Texas at Austin, 2019

Supervisor: Michael A. Cullinan

This thesis presents the design and computational optimization of a two-axis nano-positioning stage. The devised stage relies on double parallelogram flexure bearings with under-constraint eliminating linkages to enable motion in the primary degrees-of-freedom. The structural parameters of the underlying flexures were optimized to provide a large-range and high bandwidth with sub-micron resolution while maintaining a compact size. A finite element model was created to establish a functional relationship between the geometry of the flexure elements and the stiffness behavior. Then, a neural network was trained from the simulation results to explore the design space with a low computational expense. The neural net was integrated with a genetic algorithm to optimize the design of the flexures for compactness and dynamic performance. The optimal solutions resulted in a reduction of stage footprint by 14% and an increase in the first natural frequency by 75% relative to a baseline design, all while preserving the same 50mm range in each axis with a factor of safety of 2. This confirms the efficacy of the proposed approach in improving stage performance through an optimization of its constituent flexures.

Table of Contents

List of Tables

List of Figures

Chapter 1: Introduction

The purpose of this research is to develop a procedure that can be used to optimize the design of a two degree-of-freedom flexure-based precision positioning stage. The proposed methods can be employed to design a mechanism that can achieve large range decoupled motion, nanometric resolution and high bandwidth, all while maintaining a compact form-factor. This can be particularly advantageous for space constrained applications such as biological imaging and desktop micro-manufacturing.

1.1 Background and Motivation

Nano-positioning has been a key enabling technology, catalyzing advances in a variety of existing and emerging domains such as scanning probe microscopy [1]–[4], semiconductor packaging and inspection [5], [6], high-density data storage [7], micro-additive manufacturing [8], [9], nano-metrology [10] and optical communication [11].

A majority of existing two degree-of-freedom (DOF) nano-positioning systems maintain their high accuracy and motion resolution over a narrow working range of just a few hundred microns in each dimension [12]. There has been an increasing effort to extend their travel for a growing number of new precision engineering applications. For example, scanning probe microscopes available currently are often constrained by a limited range, typically in the order of tens of micrometers. The ability to make nanometer resolution measurements over a broader scan range of up to several millimeters could help address metrological challenges such as in-line inspection of large substrates in the semiconductor industry or calibration of grating scales and other standards [16]. In the field of micro-additive manufacturing, there has been recent interest in developing long range nano-positioning systems to support high-throughput fabrication of microscale 3D structures. A

novel stage system was devised for laser positioning in a micro-stereolithography (μ-SLA) system, demonstrating a motion resolution of <100 nm and a millimeter scale range (see Figure 1.1) [9]. Similarly, a nano-positioner with 50 mm of travel was used for alignment and patterning of a two-inch substrate under an optical subsystem in a micro-selective laser sintering (μ-SLS) setup [8]. Large stroke nano-positioners are rapidly gaining traction and are poised to unlock a new range of possibilities.

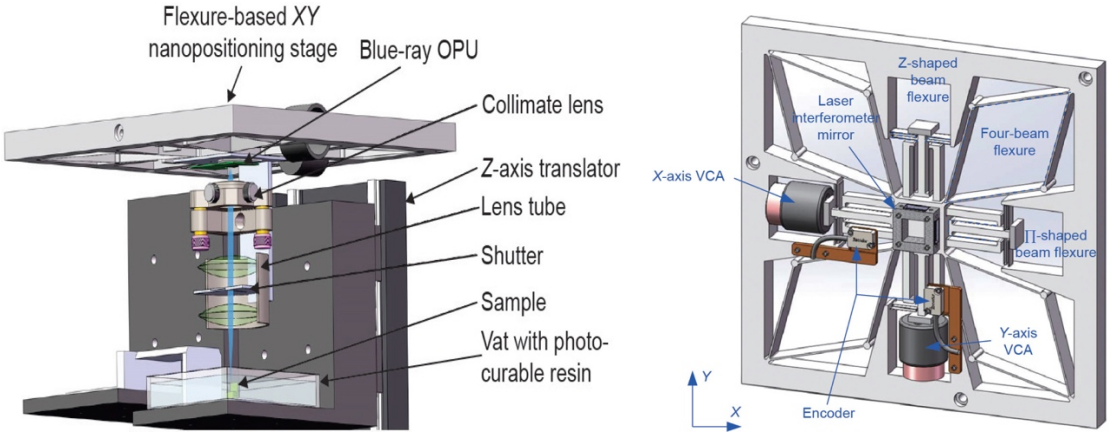

Figure 1.1: μ-SLA setup (left) with large range nano-positioner (right) [9].

Conventional stages capable of meeting the large range requirement (≈1 to 100 mm) are typically based on mechanical transmission elements such as servomotors, rack and pinion drives, ball screw actuators and rigid links. The positioning accuracy and precision of such systems is greatly compromised by non-deterministic effects such as friction and backlash that arise at the interface of mating components, making them unsuitable for micro/nanoscale applications. A common technique to overcome this limitation has been to mount a fine nano-positioner over a coarse long-range traditional motion system [18]–[20]. However, coupling two disparate mechanisms not only

necessitates more sophisticated controls due to added complexity, but also increases the size and cost of the motion system due to additional physical components [20].

Although contact-free approaches such as aerostatic bearings [22], [23] and magnetic levitation [24], [25] have been suggested to support long working ranges with high accuracy, flexure bearings have emerged as a ubiquitous choice for precision positioning systems [25]. Aerostatic bearings suffer the drawback of pressure variation from the compressor, resulting in sustained vibration, and consequent inaccuracy of stage position in the bearing direction [22]. Additionally, they are not suitable for operation in vacuum environments. Mag-lev stages rely on sophisticated feedback control for their successful implementation and are considerably expensive for laboratory scale applications [20]. Flexure bearings are compliant mechanisms that undergo elastic deformation to provide fine resolution, repeatable motion. They experience low hysteresis and eliminate the effects of friction and backlash [25], making them virtually maintenance free. Unlike traditional joints in rigid-link mechanisms, flexures often do not need to be assembled due to their monolithic fabrication, enabling design of compact, and lightweight nano-positioners [2].

Flexure-guided stages are broadly categorized as serial or parallel depending on their underlying kinematic configuration (see Figure 1.2). Serial stages are realized either by stacking actuators in series or by nesting one flexure-based nano-positioner into another. This allows for a simple construction, large working range and highly decoupled motion in each axis. However, serial systems require the base actuator to move cables and bulky actuators which drastically limit the dynamic performance of the system. Serial stage configurations also make it more challenging to measure and compensate for parasitic motion caused by cross-axis coupling. On the other hand, parallel kinematic stages are capable of operating with a high bandwidth due to the use of ground mounted actuators

that decrease the inertia of the moving mass. Although parallel kinematic stages are more susceptible to parasitic motion than their serial counterparts, feedback control can compensate for positioning errors and produce highly accurate, repeatable motion. Parallel kinematic stages are thus preferred for high speed, long range multi-axis nano-positioning applications [4].

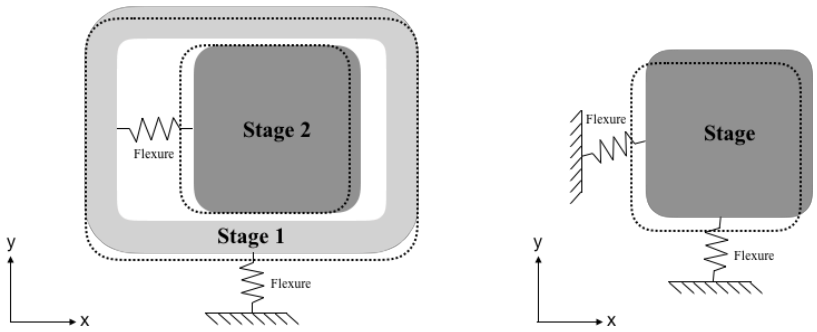

Figure 1.2: Schematic of kinematic configurations: serial (left) and parallel (right)

A number of studies have proposed conceptual designs for long-range XY flexure-based precision positioning stages use double parallelogram flexures (DPFs) as their basic building block [8], [18], [20], [26], [27]. Compared to the flexure parallelograms commonly used for linear motion, the double parallelogram configuration reduces parasitic kinematic errors using the principle of geometric reversal, providing nearly ideal linear stage motion. Additionally, modified DPFs include blade flexure linkages to couple the kinematics of the intermediate and motion stages, as shown in Figure 1.3 b. This has been shown to constrain the redundant translational degree-of-freedom of the intermediate stage [28], enhancing the stiffness and dynamic performance of the DPF. By nesting this under-constraint eliminating linkage in the dead-space of the DPF, there is no impact on the footprint. Figure 1.3 illustrates the structure and motion of both the DPF and under-constraint eliminating DPF (UE-DPF) along their primary degree-of-freedom.

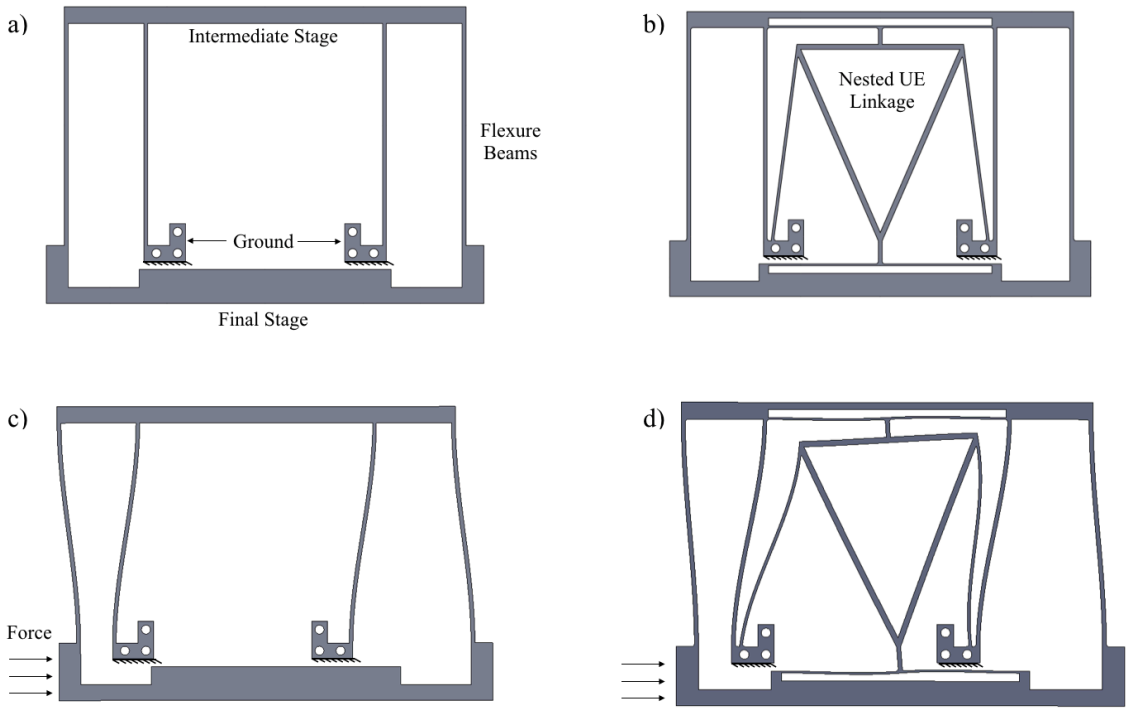

Figure 1.3: a) DPF structure b) UE-DPF structure c) DPF motion d) UE-DPF motion

The workspace offered by a stage constructed using the UE-DPFs is determined by the elastic motion range, which is in turn dependent on material properties and the geometry of the compliant members. To support longer travel ranges without significant power consumption, the UE-DPF's beams must be sufficiently compliant. At the critical beam thickness, defined by the practical tolerance of the manufacturing process, the geometric implication of slenderness is a net growth in stage footprint due to lengthening of the constituent beams. This leads to an increase in the inertia of the mechanism and decreases the first natural frequency of the system. Since a high first natural frequency is critical for fast open-loop operation, it can be seen that a large range requirement not only expands the stage footprint but also conflicts with dynamic performance.

Other design considerations such as safety factor and stress concentration determine fatigue life and stress state during stage travel. These characteristics also have an influence on the UE-DPF geometry, with more conservative designs typically resulting in an increase in stage footprint.

One of the less addressed characteristics of the XY nano-positioner is the footprint. It is expected that the stage must be compact to operate within a limited space [29], [30]. To that end, the 'area ratio' is a metric defined to quantify the workspace offered per footprint of the stage, expressed as a percentage. A higher area ratio implies a more judicious use of the space to provide the required travel. The conflicting requirements of large range, high bandwidth, low stress concentration and adequate factor of safety (FOS) make it challenging to devise a compact parallel-kinematic XY stage. The area ratios of some experimentally tested large range nano-positioners reported in literature is presented in Table 1.1.

Authors	Reference	Planar Size (mm^2)	Workspace (mm^2)	Area ratio (%)
S. Awtar and A. H. Slocum	[31]	300 X 300	5 X 5	0.03
Q. Xu	[32]	214 X 214	10.5 X 10.5	0.24
Q. Xu	[33]	120 X120	11.8 X 11.6	0.95
S. Wan and Q. Xu	[34]	244 X 244	14 X 14	0.32
N. K. Roy and M. A. Cullinan	[35]	450 X 450	50 X 50	1.15

Table 1.1: Comparison of area ratios of large range XY nano-positioners

In the past, a few different stage architectures and optimization strategies have been explored in the pursuit of millimeter, and even centimeter scale compact stages. Atwar and Parmar [20] devised a physical system layout for a parallel-kinematic stage with a high degree of motion decoupling, achieving a workspace of 10 mm x 10 mm. Further, Xu [26] improved on the state of the art by distributing planar DPFs of the stage in two stacked layers, creating a more compact structure with a similar travel range of approximately 11.7 mm in each axis. Although both studies demonstrate positioners with submicron accuracy and high resolution, they acknowledge that large motion ranges are achieved at the cost of low resonant frequency. Inspired by the use of cubical space to reduce footprint of the stage, Liu et al [29] designed a stage composed of four spatial prismatic–prismatic joints (two DPFs connected serially in space) to obtain travel range of up to 20mm x 20mm in a highly compact size. However, the conceptual stage suffers greatly from manufacturability concerns due to the high complexity of monolithic fabrication of spatial compliant mechanisms over their planar counterparts.

One of the main ideas Xu [26] proposes to improve stage characteristics is the optimization of structural parameters. Ryu et al [36] describe the use of mathematical modeling and sequential quadratic programming to select the optimal parameters of flexure-hinges in a micro-positioning XY-theta stage, providing 10 times more yaw motion than conventional counterparts. Dang et al [37] present the optimization of a stage design based on a four-lever displacement amplification mechanism. They use the Taguchi method to build the design of experiments, response surface method (RSM) to establish relationships between design variables and the output response and a genetic algorithm to maximize the first natural frequency of the stage. Huang & Dao [38] use the compliance matrix method to model the behavior of flexural hinges in an XY micro-motion stage and adopt the particle swarm optimization (PSO) algorithm to maximize the natural frequency

of the system. Although stage compactness is acknowledged to be an important design objective, most of the optimization studies [30], [36], [38], [39] in literature focus only on maximizing natural frequency and travel range.

Given their success, there is an opportunity to apply similar techniques and optimize long-range positioning systems for both footprint and bandwidth. The stage presented by Roy and Cullinan [35] has a large stroke length of 50mm, making it a suitable baseline. The geometric complexity of this UE-DPF based design suggests there is potential for structural parameter optimization.

1.2 Scope

The main contribution of this thesis is the systematic approach considered to improve the performance characteristics of a nano-positioning system through an optimization of the fundamental building blocks of the stage. Chapter 2 presents the design considerations for the underlying flexure mechanisms and the effort to model their stiffness behavior using finite element analysis. Chapter 3 describes the parametric study conducted to create a neural network, used by a genetic algorithm to optimize stiffness and footprint of the system. Chapter 4 discusses the results of the optimization, validates predictions using finite element analysis and investigates the modal performance of the optimized designs. Lastly, Chapter 5 summarizes the main findings in this thesis and outlines future work.

Chapter 2: Design and Modeling

This chapter presents the mechanism design of the nano-positioning system and the method used to model stiffness of the constituent flexures. In this study, the stage proposed by Roy and Cullinan [35] was selected to be the baseline for performance improvement. Double parallelogram flexures with nested under-constraint eliminating linkages are used as the basic building block of the stage. Since the characteristics of the system ultimately depend on the constituent flexures, the considerations guiding their design are discussed.

Further, the finite element method was employed to create a functional relationship between flexure geometry, stiffness and the resultant stress at maximum displacement. These two responses have direct consequences on the workspace, load-carrying capacity, dynamic behavior, and positioning accuracy of the entire mechanism. The chapter concludes by presenting the details of the model.

2.1 Compliant XY Stage design

2.1.1 Stage Layout

The stage developed by Roy and Cullinan [35] is a mirror symmetric arrangement of flexure modules, intended to reduce parasitic errors caused by cross-coupling. The modules are stacked in two-levels as illustrated in Figure 2.1, utilizing vertical space instead of expanding the planar area. Modules in the two-levels are arranged orthogonally, joined by coupling plates. Each monolithically fabricated module is a planar arrangement of three UE-DPFs, with the central unit connected to the motion stage and the peripheral units grounded to the base.

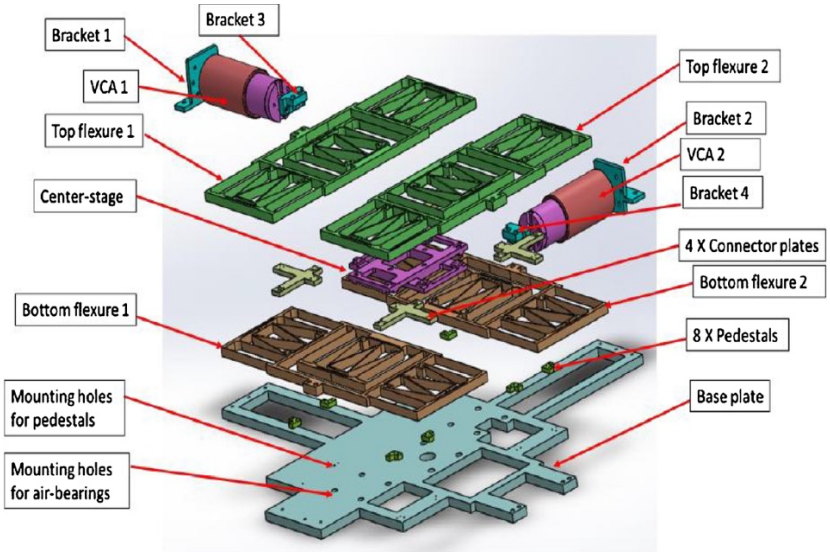

Figure 2.1: Stacked architecture of the baseline two-axis stage [35]

For stage operation, the flexures in the modules are required to deform elastically when acted upon by an external force. To enable long range travel of the center stage with high precision, voice coil actuators are a standard choice since they provide a large frictionless stroke with a fine resolution [35]. Motion along the actuation direction is guided by a set of six UE-DPFs, of which four are located at the corners of the actuated level and two are mounted in a second, parallel plane. Thus, the stiffness of the stage along each axis can be estimated to be six times that of a single UE-DPF when placed in this parallel configuration.

While the stage should permit linear motion in two perpendicular directions, it must also constrain all other degrees of freedom. By incorporating the under-constraint eliminating linkage suggested by Panas and Hopkins [28], the expected out-of-plane resonances can be pushed beyond the operating range. Due to the design freedom in geometry of these flexures, the range, kinematics, and performance of the main DOF can be designed to meet the desired specifications.

2.1.2 UE-DPF design

The shape and structure of the UE-DPF is governed both by the dimensions of the parallelogram beams as well as the nested under-constraint eliminating linkage. The main design considerations while deciding the UE-DPF geometry are as follows:

1. **Motion Range**: The range along each axis of the stage is required to be ± 25mm, providing a workspace of 50mm x 50mm. In the parallel kinematic configuration, the range of the stage is limited by the range of the UE-DPF. The travel boundaries are defined by: i) yield strength of the material, and ii) stress induced at maximum displacement, which is in turn dependent on the geometry of the flexure unit.

2. **Stiffness and Actuation Force**: The stiffness has a large influence on the static and dynamic properties of the entire stage. Six UE-DPF units are connected in parallel to guide the motion of the center stage in each motion axis. They are required to be sufficiently compliant so that the voice coil actuators can drive the stage to the desired position, especially with large displacements causing stress stiffening of flexures. Material aside, the stiffness of the UE-DPF is determined by the geometry.

3. **Natural Frequency**: In order to achieve motion control over a large bandwidth for fast operation of the nano-positioning stage, the natural frequency should be maximized. The natural frequency of the stage is proportional to the square root of the stiffness and inversely proportional to the square root of the moving mass [35], as shown in the equation below :

$$\omega_n \propto \sqrt{\frac{k}{m}}$$

where ω_n is natural frequency, k is stiffness of the stage and m is the moving mass

This implies that the dynamic performance can be improved by tailoring the geometry of the UE-DPF to increase the stiffness within the capacity of the voice coil actuators used. It is noticed that the mode shapes at the first two resonance frequencies of the stage are along the two translational axes. By increasing the in-plane stiffness, the natural frequency can be pushed out, increasing the bandwidth of the system.

4. **Stage Compactness**: The stage footprint depends on both the footprint of the individual UE-DPFs and their arrangement in space to enable two decoupled axes of motion. In the present configuration, they are stacked in two-levels to save space. However, there is an opportunity to optimize the geometric parameters of the UE-DPF to decrease their individual footprints, thus creating a more compact stage.

Since all four design considerations are tightly dependent on the geometry of the UE-DPF, it is important to examine the influence of critical design parameters in shaping the output characteristics of the stage. Based on the study of nested UE linkages [28] by Panas and Hopkins, seven variables were identified to be important to the stiffness behavior, represented in Figure 2.2.

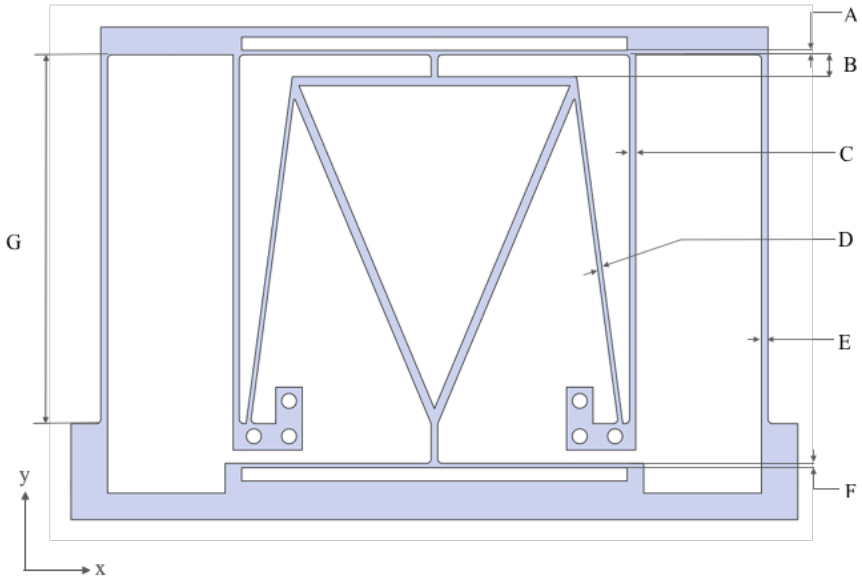

A) Top Beam Thickness (t_1)

B) Neck Length (n)

C) Inner Beam Thickness (t_{ib})

D) Slant Beam Thickness (t_{sb})

E) Outer Beam Thickness (t_{ob})

F) Bottom Beam Thickness (t_2)

G) Primary Beam Length (l)

Figure 2.2: Geometric design parameters of the UE-DPF

By selecting a combination of parameters that optimize the UE-DPF for the given design goal(s), the overall performance characteristics of the stage can be enhanced. However, before proceeding with any optimization process, the mechanism is required to be modeled so as to define an objective function that will be used for comparison of different designs.

2.2 Stiffness Modeling

Researchers have proposed several methods to model the stiffness of flexure hinges, varying in their accuracy and computational efficiency. The stiffness characteristic of a flexure mechanism has direct effects on the workspace, load-carrying capacity, dynamic behavior, and the positioning accuracy of the entire system.

Out of the available analytical methods, the compliance matrix method [40], [41] and the pseudo-rigid body method (PRBM) [42]–[44] have been extensively investigated and are widely used. The compliance matrix method is used in the kinetic analysis of planar mechanisms with flexure hinges subject to loads and small deformations. The model can be regarded a reduced finite element method, based on matrices that relate load and displacement at different points on a rigid link to the deformation of the flexure hinge in linearly elastic systems. Despite the method's efficiency, it has limitations when larger displacements are applied with reported errors of around 10% in [45] and 20% in [46]. When large displacements are involved, PRBM is often used. PRBM is an approach that takes advantage of the vast rigid-body knowledge base already available. It represents compliant bodies as a combination of rigid links and flexible joints. While the revolute joint represents the location of the center of rotation, the torsional spring represents the bending stiffness of the flexure joint. Although PRBM is a simple and comprehensible method, one limitation is that it only considers the rotational compliance of the flexure joints but treats the beams as rigid links [47]. Accounting for just one-degree of freedom, the model is prone to errors in the presence of transverse and axial loads. More recently, the nonlinear term induced by tension loading of the beams has been addressed by updated versions of PRBMs to improve the model accuracy for large displacements.

Although mathematical models are computationally cheap and might provide parametric insights, they become increasingly complicated and time consuming to develop when complex geometry such as a DPF with nested UE linkage is considered. For systems with multiple flexures and linkages, deviations between analytical and FEA results can be as high as 25% [46] due to simplifying assumptions that are made. Further, the effectiveness of any model-based experimentation and optimization cannot be guaranteed if there are large variations of modeling error across the design space.

On the other hand, computational methods such as finite element analysis (FEA) can provide more accurate assessments of a mechanism's stiffness. FEA is often used as a tool to benchmark results from analytical techniques [12], [13], [26], [30], [33]. As a versatile method, it is well suited to handle complex geometries with a variety of flexure types and loading conditions. Relying on fewer assumptions in comparison to analytical methods, FEA can treat all components as deformable, providing a far more reliable estimate of the stress, strain and the deflection of compliant mechanisms. Additionally, the tight integration of CAD with FEA tools in off-the-shelf commercial packages such as ANSYS accelerates the process of design characterization.

A finite element model was used to generate two responses for a given UE-DPF design, the stiffness and the stress state at maximum travel. Whereas stiffness is important in the determination of natural frequency, the stress state, captured by the FOS at maximum displacement indicates whether the flexures are operating in the elastic regime.

2.2.1 Modeling Setup

2.2.1.1 Geometry, meshing, and boundary conditions

The geometry used for the analysis is a cross-section of the UE-DPF along the z-axis (perpendicular to plane shown in Figure 2.2). The breadth/depth ratio of the slender flexure beams of the UE-DPF, is always found to be greater than an order-of-magnitude. Considering the application of purely bending loads, principal strain in the z-direction can be assumed as zero, yielding a plane strain condition [48]. This allows for a 2-D analysis that requires significantly less computational effort and time.

The UE-DPF was segmented to achieve a fine mesh on thin beams expected to undergo high strain, and coarser mesh on rigid structural members. A mesh convergence study was conducted to decide the trade-off between accuracy and solution time. Once determined, fixed constraints were applied to the UE-DPF mounting holes. Figure 2.3 shows the meshed 2-D model of an arbitrary design setup for the application of a prescribed displacement in the primary direction of freedom. The stiffness is estimated from a linear static simulation as the ratio of the reaction force to UE-DPF travel along the major DOF of the structure when a small prescribed displacement is applied in the tangential direction. Next, a non-linear static study is conducted with the same geometry, meshing, and constraints to predict the FOS of the UE-DPF at a large tangential displacement of 25mm.

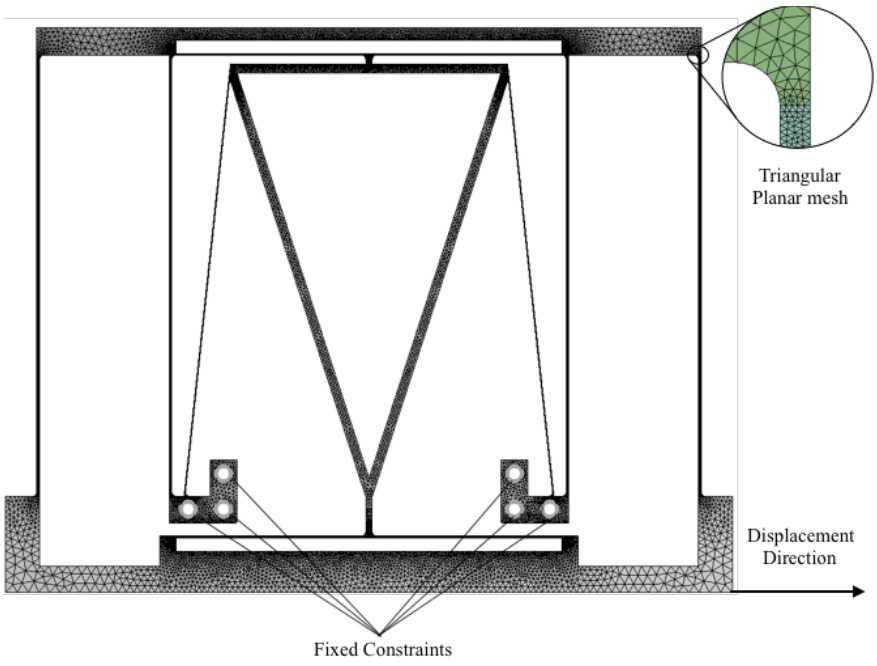

Figure 2.3: Meshed 2-D FEA model of the UE-DPF

2.2.1.2 Material Consideration

The main factors considered in the determination of the material for flexures are the yield strength, elastic modulus, density, fabrication technique and the heat treatment. It is desired to have a high stiffness-to-strength ratio to provide long range and maximize the natural frequency. Materials that exhibit a high elastic modulus-to-yield strength ratio are more attractive for applications in compliant mechanisms.

Monolithic designs are commonly adopted to reduce the assembly error of flexure units. For ease of manufacturing, it is ideal that the material is compatible with common fabrication techniques such as water jet cutting or wire electro-discharge machining. If the flexures are to be machined from plate stock, it is imperative that the internal stresses are relieved to maintain the dimensional accuracy of the flexures. Heat treatment methods adopted to eliminate the internal stress can also result in a reduction in the yield strength,

and thus a decrease in the maximum travel of the nano-positioner. Given the requirements, aluminum alloys such as 6061 and 7075 are promising for their high elastic modulus-to-yield strength ratios, fabricability and easy availability. Although a low coefficient for thermal expansion is preferred, the symmetric design configuration reduces the sensitivity of the stage to temperature variations. Al 7075 in particular can provide high strength and low internal stresses, making it a suitable material for long range precision positioning mechanism. The properties of Al 7075 are summarized in Table 2.1.

Material Property	Value
Elastic Modulus (GPa)	71.7
Yield Strength (MPa)	503
Poisson's Ratio	0.33
Density (kg/m^3)	2810

Table 2.1: Material properties of Al-7075 @ 24° C [35]

The finite element analyses detailed above are integrated with a design of experiments method so as to create metamodel that can be used to explore the design space and run optimizations rapidly. The details of the DOE, metamodeling effort and the optimization are presented in Chapter 3.

Chapter 3: Metamodel & Optimization

In this chapter, an artificial neural network is proposed to bring together the high reliability of the finite element method with the decreased computational expense of running a metamodel that is essential for exploring the design space and optimizing the UE-DPF. The presented approach applies the design of experiments to create a training dataset for the neural network. Subsequently, the neural network is used to define the objective function for parameter optimization using the genetic algorithm.

3.1 Design of Experiments (DOE)

Each design point, described by a unique combination of the variables (l, t_{ib}, t_{ob}, t_1, t_2, n, t_{sb}) introduced in Figure 2.2, picked within their bounds, generates a unique UE-DPF unit that can be analyzed. The results of the static structural analyses detailed in Chapter 2 are the in-plane stiffness and the factor of safety. Although the finite element model can accurately predict these outputs for a given design point, is impractical to use it directly in an optimization since it would involve substantial computational cost and time.

To overcome this challenge, a metamodel was employed to approximate the response from the finite element analysis. In order to ensure reliability of the metamodel, the design space was explored iteratively by parametrically varying all the inputs using a DOE. A 'Space filling' design, the Latin Hypercube was selected to vary the inputs due to its robustness and ability to scale with design variables. Latin Hypercubes are considered to be highly suitable for deterministic computer experiments [49]. The table listing all the design points considered to generate finite element simulation responses can be found in the Appendix.

By running close to five hundred experiments in ANSYS Design Xplorer, the sensitivity of the metamodel to the sampling method was reduced. Since running the design

of experiments is a one-time process, performing adequate experiments can greatly reduce the variation of errors in the ensuing metamodel.

3.2 Artificial Neural Network

After conducting a design of experiments, the next step was to use the simulation data to build an approximating model to predict the response variables. In this investigation, the technique employed was an Artificial Neural Network (ANN), created using the Deep Learning Toolbox for MATLAB.

Inspired by the biological nervous system, the ANN is a network made up of computing units called neurons arranged in different layers, interconnected by weighed edges (or synapses). Each neuron performs a set of operations and communicates the results to the neurons it is connected to. The neurons in a vertical row constitute a layer in the network, where the output of one layer becomes the input to the next. From a mathematical perspective, ANNs consist of a set of nonlinear basis functions with free parameters or weights, that need to be 'adjusted'. The 'adjustment' is a process of iteratively determining the correct value for all the weights associated with the regression using examples contained in a dataset through a process called training [50]. The neurons, once trained, allow the network to recognize patterns and predict responses without knowledge of the underlying governing equations.

Neural networks are best suited for approximating deterministic functions in regression-type applications [49]. It is widely used for function approximation and data fitting when outputs are non-linearly related to the inputs, making it ideal to model the relationship between the design parameters, the stiffness and factor of safety of the UE-DPF. In the present scenario, the trained ANN can be used to predict the response of a

linear and a nonlinear finite element analysis simultaneously in a fraction of a second, making it a powerful tool.

In order to develop the ANN, the datasets from previously conducted experimental runs are divided into training and validation sets. Out of five hundred input-output pairs in the dataset, 60% were randomly selected and used to train the network and the other 40% were used to validate the network's results. This ratio was arrived at after exploring the trade-off between overfitting and underfitting the data.

The network architecture was defined as cascade-forward with 3 neurons in each of the two hidden layers, schematically depicted with inputs and outputs in Figure 3.1.

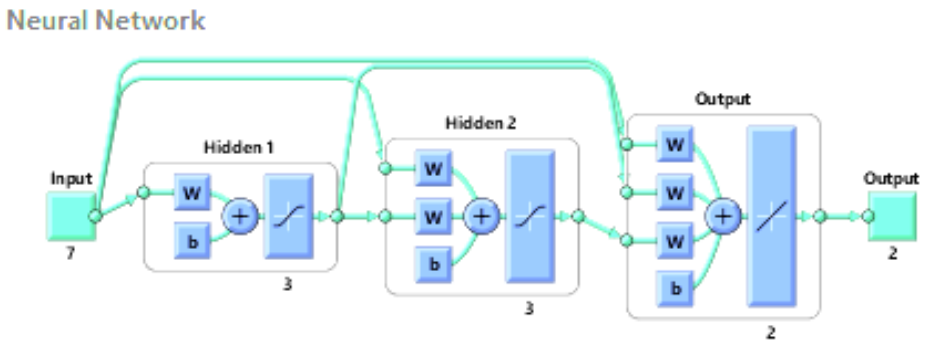

Figure 3.1: Neural Network Architecture

The performance function for cascade-forward networks is the mean square error. This refers to the average squared error between the network result and the target output. It is defined as follows:

$$\text{MSE} = \frac{1}{N}\sum_{i=1}^{N}(e_i)^2 = \frac{1}{N}\sum_{i=1}^{N}(t_i - a_i)^2$$

where *MSE* is the mean squared error, N is the number of predictions, t_i is the vector of predicted values, and a_i is vector of the expected values.

To ensure a good generalization when making predictions on test data, ten neural networks are trained, and their predictions are averaged to reduce any large errors. The mean squared errors presented in Table 3.1 are low enough to strike a balance between accuracy and generality.

Neural Net	MSE
Net 1	8.76E-04
Net 2	7.18E-04
Net 3	1.71E-03
Net 4	9.36E-04
Net 5	6.85E-04
Net 6	1.48E-03
Net 7	1.33E-03
Net 8	4.38E-04
Net 9	6.85E-04
Net 10	1.10E-03

Table 3.1: MSE of trained neural nets

On validation of the neural networks, they were used to define the fitness function of the optimization problem. Designs that satisfy the factor of safety requirement were compared by their stiffnesses and characteristic length, parameters that can be extracted from the neural net.

3.3 Optimization

Key design objectives of the considered nano-positioning stage such as large range, high natural frequency and small footprint are often contradictory, where improvement of one can deteriorate the others. The purpose of the optimization is to improve the static and dynamic characteristics of the stage relative to the baseline by careful selection of design parameters.

Classical optimization techniques such as gradient descent make use of differential calculus and require the objective function to be analytical in nature. Since the objective function in this study is defined using neural networks, a heuristic technique is necessary to solve the optimization within an acceptable time and resource cost. In this study, a genetic algorithm, created with the aid of the Global Optimization Toolbox for MATLAB, is employed for the following reasons: i) it has no requirement for derivatives, ii) it is well-suited to a discretized, high-dimensional design space, iii) it is faster than scanning techniques.

A genetic algorithm is a computational method of solving optimization problems, inspired by the concept of natural selection that underpins biological evolution. Individuals chosen from a population of design points are used as parents to produce the next filial generation. In each generation, the fitness of the designs, or the value of the objective function is evaluated and ranked. Over successive iterations, the population evolves to preserve designs that optimize the objective function, while modifying the rest (through mutation and crossover operators). The algorithm terminates when a satisfactory fitness level has been reached, or the maximum number of generations has been produced.

This study considers the range, safety factor, stiffness and footprint of the nano-positing platform for the computational optimization process. While stage moving mass can also be significant in determining the first natural resonance frequency, it does not

change appreciably with the variation of the design parameters of the UE-DPF. Therefore, stiffness is considered to be the dominant factor influencing the bandwidth of the stage. The footprint of the UE-DPF is defined here as a rectangular envelope, calculated as the product of the total length and breadth of the structure. Since the breadth is constrained by the range requirement, the footprint changes with the total length, most influenced by the primary beam length. Although there are additional performance metrics such as the cross-axis coupling error, they are not considered here. For instance, the cross-axis error can be addressed by choosing appropriate stage architectures and by using feedback control.

The objectives of the optimization are to maximize the dynamic performance, i.e. stiffness of the constituent UE-DPFs (Y_1), and simultaneously minimize footprint, characterized by the primary beam length (Y_2) while maintaining the range (Y_3) of 25mm, and a FOS of 2. The two objectives can be conveniently expressed in the fitness function as a weighted sum. The stage travel is a design specification for the current application, and the high factor of safety ensures that the stage flexures deform well within the elastic regime, preventing yielding.

The chosen design variables are: primary beam length (l); inner beam thickness (t_{ib}); outer beam thickness (t_{ob}); top beam thickness (t_1); bottom beam thickness (t_2); neck length (n); slant beam thickness (t_{sb}). The primary beam length, the length of the inner and outer flexure beams is the most important design parameter in specifying the footprint of the UE-DPF, given that the breadth is constrained by the range requirement. The upper bound for this parameter is the length of the flexure used by the existing design, 101.85mm, constraining footprint to the current size. After preliminary runs, the lower bound was set at 60mm to narrow down the design space enough to save on computational time but not exclude any optimal solutions. The lower bound for all beam thicknesses considered was fixed at 0.2mm, set by the manufacturing tolerance of the wire electric discharge machining

process. The upper bound was set such that thicknesses beyond them would increase the stiffness of the platform and increase the possibility of yielding the material at maximum travel. The neck length was bounded between 2mm and 4mm. The design variables are allowed to vary in discrete steps within their bounds for ease of manufacturability. Apart from the dimensions discussed, the width of all the beams was considered constant at 12.7 mm, since the UE-DPF is planned to be machined out of half inch Al 7075 plate stock.

In the standard mathematical format, the optimization can be stated as follows:

$$\text{Minimize: } W_1 * (Y_2 / 101.85) - W_2 * (Y_1 / 105)$$

subject to:

$$Y3 = 25 \text{ mm}$$

$$\frac{\sigma max}{\sigma y} \geq 2$$

$$Y1 \geq 105 \text{ N/m}$$

$$60 \text{ mm} \leq l \leq 101.85 \text{ mm}$$

$$0.2 \text{ mm} \leq t_1 \leq 0.7 \text{ mm}$$

$$0.2 \text{ mm} \leq t_2 \leq 0.7 \text{ mm}$$

$$0.2 \text{ mm} \leq t_{ib} \leq 0.5 \text{ mm}$$

$$0.2 \text{ mm} \leq t_{ob} \leq 0.5 \text{ mm}$$

$$0.2 \text{ mm} \leq t_{sb} \leq 0.5 \text{ mm}$$

$$2 \text{ mm} \leq n \leq 4 \text{ mm}$$

In this paper, the weights or priorities of two design objectives are adjusted based on the relative importance of each. After computational analysis, potential candidates are generated and compared to find optimal solutions. The results are presented, verified and discussed in the next chapter. The following flowchart, Figure 3.2 summarizes the proposed optimization approach

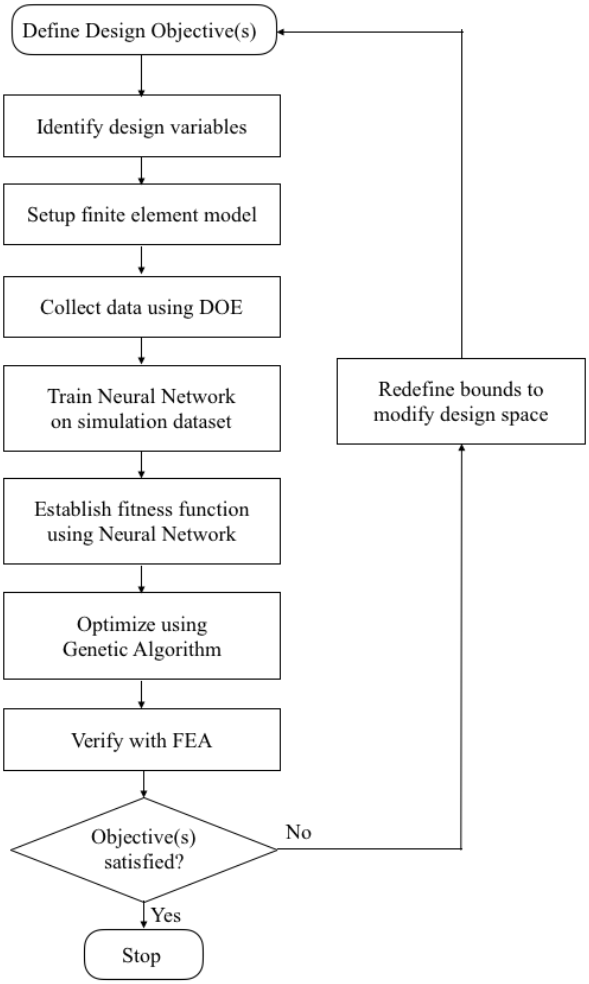

Figure 3.2: Proposed Computational Optimization Approach

Chapter 4: Results and Discussion

Chapter 4 discusses the results of the optimization conducted on the UE-DPF structure. Two design solutions of particular interest are presented and verified using FEA simulations. Subsequently, modal analysis is performed on stages constructed with these optimized UE-DPF units, and their dynamic properties are compared with the baseline.

4.1 Optimal designs

The optimization process was conducted by evaluating fitness based on a weighted sum of the design goals. Although several optimal solutions can be found, two corner cases are presented here. The first design solely prioritizes the minimization of footprint ($W_1 = 1$, $W_2 = 0$) while the second prioritizes the maximization stiffness ($W_1 = 0$, $W_2 = 1$) while meeting all the performance requirements of the baseline stage [35]. The dimensions of the two optimized UE-DPFs are compared with the existing design in Table 4.1.

		Baseline Design	Optimal Design A (Min. Footprint)	Optimal Design B (Max. Stiffness)
Input Parameters	l (mm)	101.85	81.1	99.8
	t_{ib} (mm)	0.3	0.3	0.6
	t_{ob} (mm)	0.3	0.4	0.7
	t_1 (mm)	0.35	0.2	0.325
	t_2 (mm)	0.35	0.2	0.4
	n (mm)	6.73	2	2
	t_{sb} (mm)	0.3	0.2	0.2
Output Parameters	FOS	1.91	2.00	2.14
	Stiffness (N/m)	105.20	113.55	313.95
	Footprint (mm^2)	20876.9	18001.5	21087.0

Table 4.1: Comparison of geometric parameters of optimal and baseline UE-DPF designs

The footprint optimizing UE-DPF design was found to be 13.8 % smaller than the baseline. The major factor that contributed to the reduction of the size is the decrease in primary beam length (l), the perpendicular distance between the intermediate and motion stage. The result of optimizing UE-DPF for footprint can be visualized in Figure 4.1. On the other hand, the design that maximizes in-plane stiffness is within 1% of the current size and is nearly 200% stiffer than the baseline.

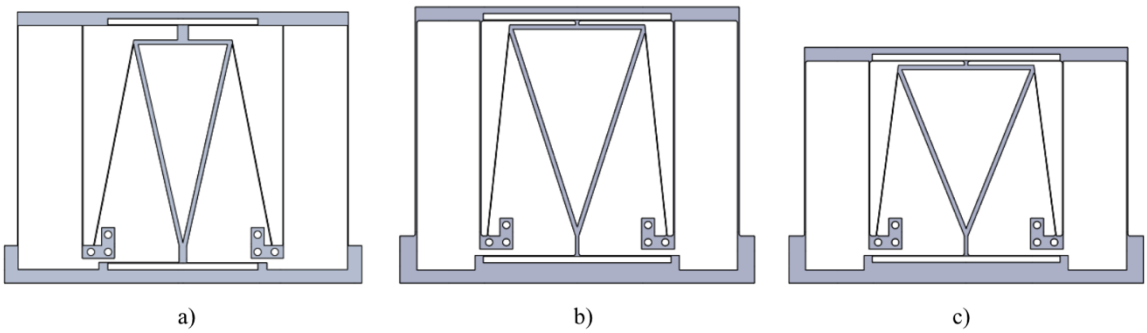

Figure 4.1: Comparison of optimized UEDPF structures with the baseline design:
a) Baseline b) Stiffness-optimized design c) Footprint-optimized design

Since the optimal design candidates were derived from a neural network, an approximation of the finite element model, they need to be validated against FEA. Table 4.2 compares stiffness and FOS results from the proposed approach and FEA.

		Predicted Result	FEA	Error %
FOS	Optimal Design A	2.01	2.08	3.37
	Optimal Design B	2.14	1.97	8.62
Stiffness	Optimal Design A	113.55	107.29	5.83
	Optimal Design B	313.95	317.50	1.12

Table 4.2: Validation of optimal designs using FEA

The comparison indicates acceptable deviation of within 9% of the results from FEA. Therefore, the proposed approach is adequate to approximate the relationship between the input and output parameters of the system. By minimizing computational time, it allows for efficient optimization the structural parameters of the UE-DPF.

Further, the optimal design candidates are integrated into a stage configuration to determine their impact on compactness and natural frequency of the nano-positioner. Figure 4.2 is a comparison of the baseline with the footprint-optimized stage. It was found that the footprint-optimized design results in a total 14% reduction of the baseline's footprint. The improvement was enabled by generating the stage with compact UE-DPFs which can be more tightly packed in a stacked modular structure.

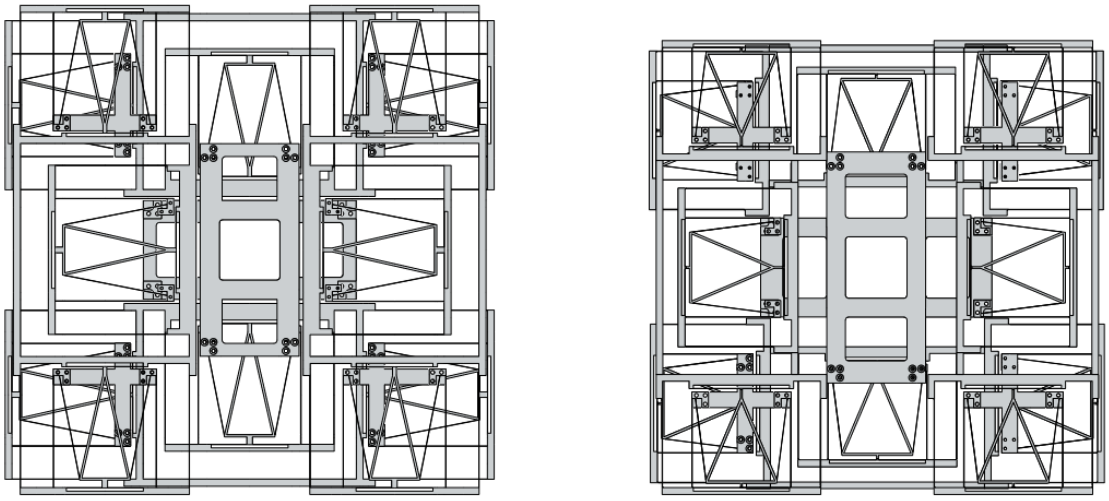

Figure 4.2: Comparison of baseline (left) with footprint-optimized stage (right)

Finally, the first six natural frequencies of the optimized stages were estimated from a modal analysis and compared with the baseline in Table 4.3 below.

	Baseline Stage Design	Footprint-Optimized Stage Design	Stiffness-Optimized Stage Design
Mode 1 (Hz)	3.57	3.85	6.26
Mode 2 (Hz)	3.57	3.86	6.26
Mode 3 (Hz)	66.39	81.30	74.39
Mode 4 (Hz)	78.39	84.52	76.03
Mode 5 (Hz)	80.33	98.52	86.04
Mode 6 (Hz)	84.11	108.38	92.28

Table 4.3: Comparison of the natural frequencies of the optimal stages with the baseline

While the footprint-optimized stage and the baseline have approximately the same open-loop bandwidth, the first resonance frequency of the stiffness-optimized stage is 75% higher, or 1.75X the baseline. This improvement is attributed to the UE-DPF's stiffness, 3X of the baseline. This corroborates the initial analysis where the first resonance frequency was expected to be directly proportional to the square root of the in-plane stiffness ($\sqrt{3} \cong 1.75$). Since the footprint-optimized stage and the baseline have very similar in-plane stiffnesses, their first natural frequency is almost identical.

The first six modes of the three stages under consideration can be visualized in the following figures (Figure 4.3, Figure 4.4 and Figure 4.5)

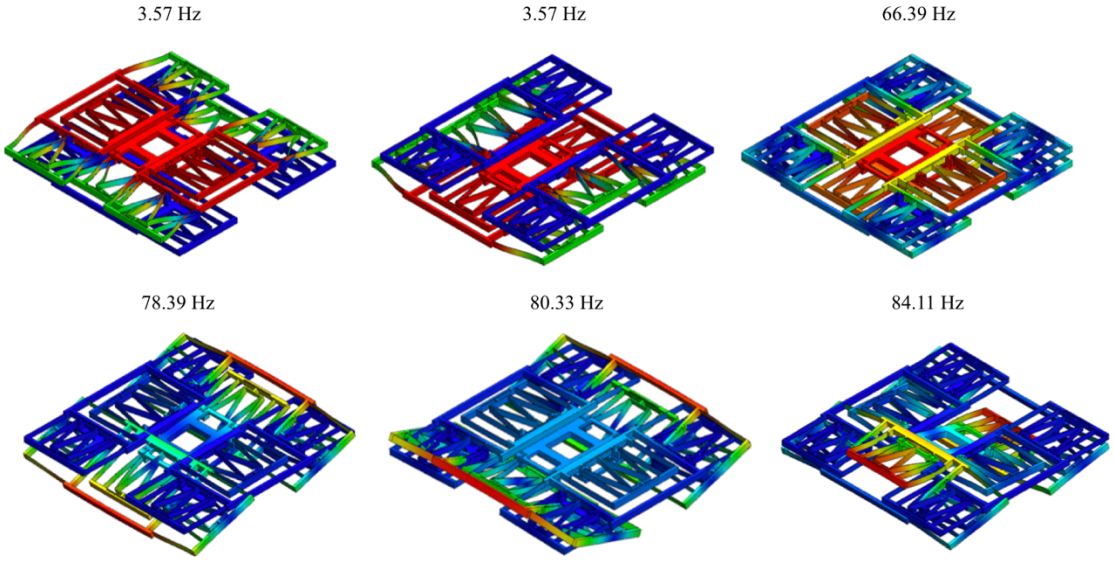

Figure 4.3: The first 6 mode shapes of the baseline stage

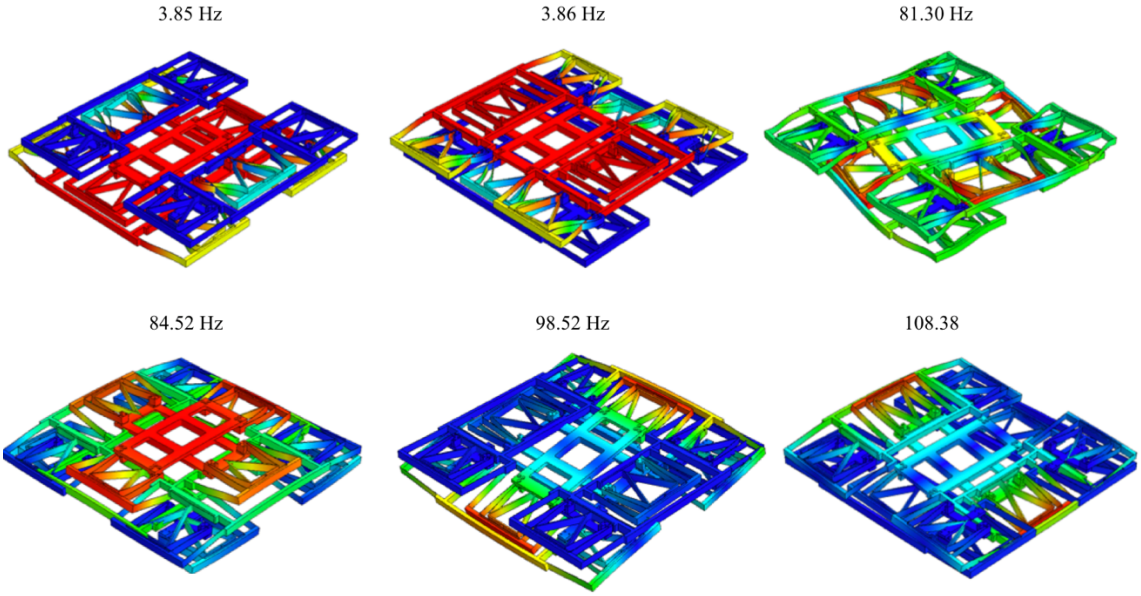

Figure 4.4: The first 6 mode shapes of the foot-print optimized stage

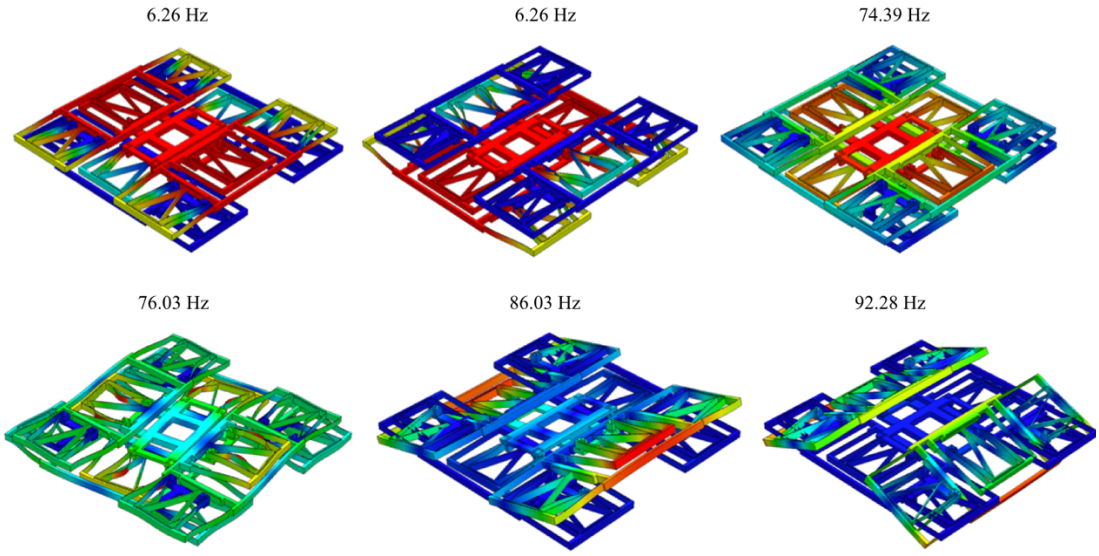

Figure 4.5: The first 6 mode shapes of the stiffness-optimized stage

From Figures 4.3-4.5, the first two modes of the stage are always in-plane translations along the two primary degrees-of-freedom of the center platform. These modes can be compensated for with feedback control. The third mode shape in the baseline & stiffness-optimized stage, identical to the fourth mode in the footprint-optimized stage, is a translation of the center stage along the z-axis. The third mode of the footprint-optimized stage is an in-plane twisting of the structure about the z-axis, causing parasitic rotation of the center stage. Since the stiffness-optimized design has a higher in-plane stiffness, the twisting mode is pushed out. The fifth and sixth modes for all stages are out-of-plane bending motions of the flexure modules. Although resonances beyond the second mode cannot be controlled by stage actuators, they occur at frequencies well outside of the desired bandwidth (25 Hz) and should not affect the performance during operation.

In summary, the optimization resulted in positioning platforms that can i) increase the safety factor of the design by 3-9% ii) reduce the footprint by 14% and iii) enhance the first natural frequency by 75% compared to the baseline.

Chapter 5: Conclusions and Future Work

This chapter recapitulates the main outcomes and discusses the limitations of the present study. Further, it outlines opportunities for future work in this area.

5.1 Conclusions

The main objective of this research is to develop a systematic approach to enhance the performance characteristics of flexure-based XY nano-positioning systems. The geometry of the underlying compliant mechanisms has a strong influence on the static and dynamic properties of the system. Therefore, significant improvements can be realized through structural optimization of the basic building blocks of the stage, the double parallelogram flexure. Optimization can assist in exploring the trade-off between conflicting objectives such as long-range, high bandwidth, and compact size, enabling design for a variety of precision positioning applications.

The work presented here addresses the growing need for two-axis nano-positioning systems that maintain high motion quality over millimeter travel ranges and fit into a desktop-size form factor. The first step in the development of such a system was the identification of a baseline that has the potential to satisfy the above requirements. A DPF-based parallel-kinematic design was chosen in the interest of achieving a long-range motion with low inertia, high bandwidth, and identical dynamics in both the X & Y directions. Additionally, the design incorporated a nested linkage to eliminate under-constraint in the flexure units, pushing out parasitic eigenfrequencies that limit the maximum operating speed of the mechanism. The individual flexure units were arranged in modules and stacked in two parallel planes, utilizing space efficiently. Although the baseline has several merits, the long travel range of the central platform came at the cost of enlarging the flexure modules, increasing the overall size and thus, the inertia of the

mechanism. The increase in inertia is accompanied by a consequent decrease in natural frequency, proving detrimental to the bandwidth of the stage.

In order to overcome this challenge through design optimization, the first step was to model the basic building block of the stage, the UE-DPF. Due to the complexity of UE-DPF geometry, a computational method was chosen over traditional analytical approaches to estimate the output characteristics: in-plane stiffness and resultant stress at maximum displacement. Whereas the first natural frequency is directly proportional to the square root of in-plane stiffness, the resultant stress at maximum displacement can determine if the flexures deform strictly in the elastic regime. Both linear and non-linear finite element models were employed to accurately capture the stress-strain behavior of the UE-DPF under different quasistatic loading conditions. Using the plane-strain assumption, the analyses were reduced to 2D FEA, enabling a design of experiments to understand the relationship between the geometry of the structure and output characteristics within an acceptable time and resource cost.

Next, an artificial neural network was trained on the simulation results generated from the design of experiments. The neural network was used to approximate the response of the finite element model to further reduce computational expense for an efficient exploration of the design space. Once validated for model accuracy, it was integrated with a genetic algorithm to identify candidate solutions that would optimize the natural frequency and footprint of the UE-DPF.

The design goals were adjusted to reflect their relative priority in the optimization. The optimal solutions included: i) the stiffness-maximizing design, resulting in a stage with a 75% increase in the first resonant frequency ii) a footprint-minimizing design, reducing the stage area by 14% compared to the baseline. Through identification of key design

variables, modeling and optimization, a compact stage with a long motion range and good dynamic performance has been achieved.

Beyond the improvement of the baseline design, this work has highlighted the advantages of metamodel-based computational structural optimization in enhancing the performance characteristics of a nano-positioning stage right. The proposed approach can be used to design flexure units tailored for application in novel configurations.

5.2 Future Work

The goal of this project was to conduct an optimization on the existing design of the two-axis nano-positioner [35] to provide a long range of 50mm while improving the dynamic performance and decreasing the stage footprint. Opportunities for future developments are in three key areas: 1) extension of the scope of the study to include additional design variables and objectives, 2) exploration of novel configurations for the arrangement of optimal flexure units, and 3) sensitivity analysis, fabrication and testing of a physical prototype

1) The current study considers the variation of seven design parameters of the UE-DPF on the output stiffness and equivalent stress at maximum stage displacement. The geometry of the nested linkage introduces several variables that could influence the static and dynamic characteristics of the structure. Of these, two important dimensions, the slant beam thickness and the neck length have been studied. The sensitivity of the response to other design parameters such as the angle of the slant beams should be investigated. In addition, the plate thickness that the UE-DPFs are cut from can be incorporated into the optimization to estimate the out-of-plane stiffness and load-carrying capacity of the stage.

2) The proposed optimization approach can be tailored to generate the design parameters that minimize the footprint of the UE-DPF for a given range requirement. However, there is still a challenge in conceptualizing the overall arrangement, distribution and utilization of these basic building blocks to construct a stage with large workspace, decoupled motion, symmetric dynamics in both axes and a compact form-factor. Novel configurations that reduce the footprint and utilize cubical space can be investigated to address this.
3) The main limitation of the proposed stage is the sensitivity of the performance to manufacturing and assembly. Although Wire-EDM (Electro Discharge Machining) and drilling have a tolerance of ±10 μm, along with assembly errors and the superposition of the tolerances due to the large number of flexure beams used, the actual response characteristics of the nano-positioner could differ from the design. Therefore, a sensitivity analysis should be performed, and the design should further be fine-tuned for robustness. The final step would be the fabrication and testing of a prototype to assess performance and validate the results of the design optimization.

Appendix

The simulation data obtained from the design of experiments is tabulated below. Seven parameters were varied, and the stiffness and factor of safety were determined using FEA.

	Primary Length	Half T_IB	Half T_OB	T_1	T_2	N	T_SLB	FOS	Stiffness
D1	70.72	0.20	0.18	0.28	0.23	2.30	0.28	1.12	340.40
D2	92.40	0.26	0.29	0.43	0.28	2.90	0.33	1.60	336.16
D3	68.64	0.18	0.19	0.50	0.46	4.97	0.44	0.61	831.23
D4	83.76	0.24	0.32	0.24	0.26	2.61	0.36	1.29	447.67
D5	81.44	0.33	0.23	0.32	0.20	4.61	0.46	0.74	991.07
D6	99.76	0.26	0.18	0.40	0.43	2.72	0.49	1.19	403.70
D7	91.84	0.35	0.13	0.20	0.21	2.23	0.36	1.11	583.45
D8	68.48	0.12	0.22	0.39	0.41	3.22	0.43	0.65	646.18
D9	96.16	0.19	0.14	0.34	0.24	3.08	0.36	1.61	187.21
D10	85.76	0.27	0.11	0.24	0.33	3.51	0.43	0.95	523.75
D11	85.20	0.20	0.14	0.21	0.45	3.40	0.32	1.38	240.60
D12	102.00	0.23	0.19	0.33	0.46	3.22	0.31	2.06	173.40
D13	73.52	0.17	0.24	0.43	0.21	3.15	0.48	0.70	757.62
D14	89.84	0.32	0.10	0.46	0.21	2.62	0.23	1.26	447.32
D15	86.32	0.21	0.33	0.48	0.32	4.49	0.45	0.98	529.20
D16	74.88	0.16	0.30	0.50	0.39	4.32	0.39	0.80	497.63
D17	66.72	0.28	0.26	0.21	0.38	3.47	0.28	0.83	869.35
D18	92.48	0.25	0.26	0.22	0.48	2.33	0.46	1.14	452.97
D19	85.92	0.17	0.21	0.34	0.29	4.35	0.35	1.35	238.87
D20	72.08	0.28	0.20	0.39	0.42	4.79	0.45	0.63	1093.58
D21	90.64	0.17	0.14	0.21	0.50	2.97	0.30	1.81	151.00
D22	101.12	0.22	0.34	0.48	0.44	4.31	0.47	1.26	360.06
D23	94.88	0.32	0.15	0.35	0.46	2.93	0.31	1.36	435.76
D24	97.20	0.29	0.25	0.46	0.38	2.25	0.21	1.94	297.60
D25	95.04	0.17	0.26	0.27	0.46	2.86	0.42	1.35	257.21
D26	88.16	0.34	0.33	0.30	0.25	4.37	0.22	1.34	607.96
D27	75.36	0.25	0.15	0.45	0.49	3.01	0.30	1.05	502.28
D28	85.28	0.19	0.25	0.31	0.37	4.59	0.41	1.07	376.55
D29	84.64	0.30	0.24	0.29	0.45	4.30	0.36	1.06	578.16
D30	84.08	0.30	0.30	0.21	0.21	3.55	0.28	1.24	548.99

D31	88.96	0.29	0.34	0.36	0.49	4.53	0.32	1.40	512.05
D32	78.72	0.30	0.33	0.49	0.45	3.37	0.39	0.96	870.51
D33	87.60	0.29	0.18	0.30	0.32	2.62	0.46	0.94	610.25
D34	87.52	0.21	0.20	0.50	0.39	2.10	0.22	2.05	186.40
D35	74.00	0.11	0.16	0.28	0.23	3.80	0.24	1.34	121.09
D36	99.20	0.33	0.18	0.35	0.44	4.30	0.33	1.41	422.51
D37	84.56	0.35	0.14	0.37	0.21	3.93	0.33	0.98	733.77
D38	67.20	0.33	0.26	0.41	0.27	2.57	0.38	0.65	1505.91
D39	103.28	0.14	0.21	0.28	0.39	4.72	0.31	2.09	97.58
D40	82.72	0.21	0.22	0.31	0.32	2.90	0.24	1.72	225.17
D41	93.20	0.34	0.12	0.25	0.31	2.42	0.39	1.12	564.77
D42	95.92	0.18	0.12	0.31	0.30	3.02	0.49	1.12	333.39
D43	88.80	0.27	0.16	0.28	0.39	2.50	0.30	1.41	336.65
D44	99.52	0.20	0.19	0.30	0.40	3.68	0.40	1.51	223.05
D45	100.16	0.34	0.29	0.49	0.39	2.38	0.27	1.70	431.79
D46	84.88	0.17	0.13	0.38	0.31	2.12	0.30	1.57	181.41
D47	65.60	0.23	0.14	0.26	0.48	3.61	0.37	0.66	805.93
D48	75.84	0.18	0.14	0.42	0.35	4.04	0.48	0.71	684.11
D49	84.40	0.34	0.21	0.23	0.36	4.03	0.33	0.99	715.11
D50	66.00	0.22	0.24	0.39	0.22	3.64	0.46	0.59	1112.74
D51	72.56	0.16	0.30	0.21	0.22	4.70	0.37	0.84	492.82
D52	71.36	0.12	0.34	0.41	0.24	4.25	0.39	0.69	559.60
D53	84.72	0.22	0.17	0.25	0.27	2.80	0.23	1.62	214.56
D54	67.92	0.27	0.22	0.29	0.32	2.08	0.46	0.61	1221.22
D55	78.24	0.32	0.27	0.27	0.44	2.72	0.47	0.72	1122.99
D56	80.16	0.29	0.25	0.33	0.39	4.09	0.28	1.11	579.03
D57	86.96	0.26	0.33	0.33	0.23	2.31	0.21	1.69	349.17
D58	100.72	0.33	0.34	0.44	0.33	3.71	0.36	1.50	472.83
D59	76.80	0.11	0.27	0.26	0.27	2.12	0.38	0.97	327.35
D60	79.44	0.14	0.15	0.41	0.29	4.13	0.36	1.07	280.69
D61	80.32	0.33	0.27	0.24	0.38	2.87	0.41	0.87	904.11
D62	98.40	0.18	0.20	0.37	0.27	4.46	0.34	1.82	155.76
D63	82.24	0.26	0.30	0.23	0.21	4.19	0.27	1.39	422.08
D64	104.48	0.19	0.16	0.42	0.45	3.92	0.29	2.43	118.06
D65	66.40	0.30	0.31	0.25	0.50	3.30	0.25	0.87	1066.45
D66	90.48	0.27	0.17	0.20	0.50	2.26	0.33	1.39	359.21
D67	69.44	0.14	0.30	0.28	0.34	3.88	0.29	0.85	352.64
D68	95.52	0.33	0.19	0.34	0.48	2.39	0.48	1.05	613.68
D69	95.20	0.15	0.34	0.22	0.40	2.78	0.45	1.21	300.99

D70	66.24	0.27	0.33	0.42	0.28	2.86	0.50	0.53	1614.59
D71	90.00	0.14	0.12	0.46	0.34	2.80	0.34	1.55	157.92
D72	80.64	0.29	0.17	0.31	0.36	3.28	0.22	1.14	459.37
D73	71.76	0.34	0.29	0.31	0.32	4.18	0.31	0.78	1207.62
D74	92.00	0.33	0.23	0.38	0.32	4.78	0.45	0.97	687.31
D75	89.60	0.15	0.34	0.45	0.35	2.58	0.42	1.11	327.59
D76	80.40	0.21	0.25	0.43	0.41	4.36	0.30	1.24	324.90
D77	100.08	0.32	0.16	0.41	0.30	3.74	0.27	1.59	335.43
D78	101.28	0.16	0.15	0.45	0.48	4.73	0.32	1.90	124.54
D79	78.40	0.13	0.34	0.21	0.26	2.52	0.41	0.91	432.47
D80	102.64	0.25	0.16	0.36	0.41	3.80	0.39	1.56	255.24
D81	71.44	0.14	0.12	0.25	0.43	2.53	0.31	1.04	258.25
D82	101.36	0.24	0.18	0.38	0.31	4.61	0.35	1.70	219.19
D83	103.52	0.16	0.20	0.35	0.42	3.91	0.30	2.16	102.15
D84	90.80	0.15	0.12	0.46	0.28	4.09	0.28	1.84	121.10
D85	81.76	0.12	0.10	0.42	0.28	3.36	0.45	0.94	384.53
D86	86.80	0.27	0.17	0.48	0.44	4.44	0.25	1.39	350.15
D87	73.44	0.24	0.25	0.27	0.45	3.48	0.41	0.79	746.94
D88	82.48	0.16	0.21	0.29	0.31	4.54	0.27	1.49	170.38
D89	91.68	0.19	0.14	0.34	0.30	4.38	0.40	1.28	255.75
D90	73.20	0.29	0.34	0.43	0.26	3.42	0.38	0.86	977.36
D91	65.04	0.15	0.25	0.26	0.46	2.32	0.29	0.83	389.05
D92	101.76	0.16	0.24	0.23	0.23	3.59	0.35	1.99	132.64
D93	104.32	0.23	0.33	0.30	0.26	3.24	0.25	2.72	167.13
D94	104.64	0.26	0.22	0.30	0.48	3.05	0.26	2.33	181.82
D95	83.04	0.19	0.24	0.33	0.23	4.55	0.34	1.27	296.43
D96	80.96	0.27	0.28	0.36	0.27	4.63	0.44	0.84	754.68
D97	86.56	0.34	0.20	0.35	0.40	4.03	0.26	1.08	632.14
D98	97.44	0.28	0.19	0.32	0.47	3.70	0.44	1.20	420.58
D99	82.96	0.30	0.26	0.32	0.40	4.71	0.22	1.20	512.71
D100	72.16	0.13	0.26	0.34	0.43	2.73	0.35	0.86	361.83
D101	70.80	0.18	0.32	0.28	0.42	2.77	0.43	0.68	758.14
D102	90.96	0.18	0.30	0.23	0.41	2.96	0.34	1.48	220.30
D103	68.24	0.10	0.31	0.30	0.36	3.84	0.37	0.67	532.85
D104	70.96	0.22	0.25	0.43	0.33	4.76	0.35	0.86	611.17
D105	103.36	0.28	0.24	0.25	0.21	2.54	0.31	1.93	236.86
D106	78.32	0.15	0.12	0.23	0.29	3.38	0.40	0.95	347.97
D107	72.96	0.19	0.31	0.35	0.35	2.14	0.37	0.88	525.73
D108	74.72	0.26	0.19	0.43	0.48	2.17	0.49	0.68	975.23

D109	95.28	0.18	0.34	0.40	0.31	2.44	0.26	1.73	169.75
D110	71.20	0.21	0.16	0.25	0.38	2.83	0.29	1.05	392.94
D111	83.28	0.32	0.14	0.45	0.38	4.81	0.39	0.88	743.69
D112	82.80	0.13	0.22	0.46	0.47	3.86	0.27	1.30	157.42
D113	94.56	0.26	0.18	0.47	0.37	2.96	0.22	1.86	244.18
D114	91.52	0.25	0.15	0.36	0.37	3.01	0.21	1.78	221.21
D115	69.04	0.22	0.35	0.29	0.40	2.75	0.21	1.00	525.52
D116	98.32	0.27	0.25	0.44	0.24	2.51	0.23	2.05	249.22
D117	97.68	0.28	0.19	0.37	0.26	4.36	0.48	1.10	462.77
D118	76.56	0.21	0.13	0.47	0.29	2.32	0.45	0.80	612.59
D119	88.64	0.10	0.11	0.38	0.28	4.85	0.43	1.11	272.44
D120	85.12	0.22	0.17	0.25	0.33	4.96	0.21	1.62	197.66
D121	73.68	0.12	0.11	0.42	0.35	3.62	0.40	0.84	403.16
D122	68.16	0.22	0.12	0.39	0.43	2.68	0.30	0.90	508.45
D123	91.44	0.18	0.12	0.46	0.42	4.46	0.35	1.45	219.19
D124	91.04	0.31	0.23	0.24	0.44	3.37	0.22	1.40	423.94
D125	78.48	0.16	0.24	0.43	0.38	3.75	0.22	1.32	189.51
D126	104.96	0.23	0.33	0.22	0.44	2.81	0.30	2.29	192.15
D127	83.20	0.14	0.27	0.26	0.41	3.85	0.23	1.40	139.36
D128	98.00	0.24	0.13	0.43	0.20	3.70	0.22	2.07	160.70
D129	73.92	0.32	0.34	0.26	0.38	3.18	0.45	0.69	1319.11
D130	70.56	0.14	0.21	0.29	0.41	4.02	0.23	1.06	193.30
D131	95.44	0.34	0.33	0.47	0.31	3.95	0.46	1.08	679.64
D132	73.76	0.32	0.18	0.48	0.20	4.12	0.22	0.84	803.45
D133	74.16	0.11	0.11	0.36	0.25	3.76	0.20	1.47	90.43
D134	72.80	0.12	0.32	0.42	0.46	2.26	0.23	0.92	231.66
D135	81.60	0.12	0.27	0.42	0.46	4.24	0.40	0.94	350.00
D136	87.12	0.30	0.22	0.28	0.32	4.68	0.40	1.00	586.54
D137	66.56	0.18	0.11	0.49	0.35	3.23	0.29	0.92	400.43
D138	73.12	0.27	0.18	0.32	0.29	2.08	0.32	0.90	645.99
D139	98.72	0.35	0.23	0.33	0.30	2.63	0.31	1.45	466.66
D140	82.00	0.25	0.33	0.39	0.25	4.70	0.49	0.81	796.59
D141	102.08	0.24	0.31	0.46	0.41	4.58	0.27	2.26	208.78
D142	103.44	0.33	0.11	0.40	0.29	4.82	0.20	1.58	304.35
D143	69.36	0.27	0.11	0.42	0.22	3.82	0.27	0.83	692.10
D144	84.16	0.34	0.21	0.25	0.31	4.85	0.39	0.88	829.93
D145	85.68	0.16	0.19	0.32	0.46	3.14	0.33	1.38	207.72
D146	104.08	0.31	0.29	0.37	0.38	4.63	0.42	1.42	398.41
D147	79.36	0.23	0.26	0.42	0.22	3.23	0.41	0.96	533.84

D148	103.04	0.13	0.28	0.41	0.43	3.34	0.39	1.61	162.23
D149	75.76	0.20	0.15	0.34	0.39	4.10	0.42	0.85	550.78
D150	99.12	0.17	0.34	0.39	0.26	2.05	0.46	1.32	293.13
D151	87.84	0.25	0.25	0.20	0.31	4.18	0.40	1.12	439.51
D152	89.36	0.31	0.24	0.33	0.42	3.53	0.46	0.96	665.57
D153	96.40	0.13	0.13	0.41	0.25	2.29	0.20	2.63	50.95
D154	80.24	0.28	0.20	0.20	0.36	3.67	0.48	0.73	842.96
D155	75.04	0.28	0.12	0.20	0.39	3.65	0.24	0.97	569.53
D156	85.52	0.20	0.25	0.49	0.47	3.65	0.33	1.30	297.10
D157	96.48	0.30	0.16	0.20	0.28	4.05	0.48	1.06	520.93
D158	96.24	0.24	0.20	0.33	0.34	3.53	0.24	2.01	190.65
D159	103.12	0.14	0.32	0.45	0.23	2.55	0.48	1.36	260.26
D160	88.56	0.31	0.13	0.30	0.40	2.34	0.29	1.27	447.81
D161	86.16	0.12	0.31	0.27	0.24	4.94	0.45	0.97	388.54
D162	79.60	0.19	0.14	0.38	0.33	2.92	0.36	1.09	322.54
D163	87.68	0.14	0.18	0.37	0.28	3.52	0.37	1.29	209.28
D164	81.36	0.24	0.21	0.49	0.24	2.33	0.27	1.38	337.76
D165	95.12	0.10	0.30	0.36	0.43	3.11	0.40	1.34	208.20
D166	100.88	0.17	0.32	0.40	0.45	2.47	0.23	1.97	120.97
D167	76.40	0.27	0.13	0.34	0.25	2.71	0.49	0.69	908.51
D168	86.48	0.26	0.24	0.37	0.22	4.07	0.29	1.38	361.89
D169	65.20	0.33	0.18	0.48	0.43	4.42	0.37	0.52	1643.49
D170	99.04	0.11	0.17	0.49	0.24	4.87	0.43	1.38	205.87
D171	102.48	0.29	0.23	0.36	0.35	3.54	0.39	1.50	327.44
D172	85.04	0.16	0.21	0.35	0.49	2.48	0.45	1.03	373.60
D173	95.76	0.18	0.18	0.27	0.40	3.61	0.27	2.23	119.98
D174	90.32	0.14	0.32	0.37	0.48	4.11	0.43	1.07	333.68
D175	78.08	0.13	0.25	0.42	0.40	3.12	0.40	0.89	387.71
D176	83.60	0.34	0.27	0.30	0.23	3.56	0.42	0.88	872.67
D177	98.80	0.21	0.34	0.26	0.23	4.75	0.30	1.88	193.78
D178	75.28	0.32	0.15	0.24	0.38	2.66	0.32	0.84	850.43
D179	78.88	0.25	0.15	0.42	0.44	3.58	0.29	1.15	424.01
D180	66.96	0.27	0.29	0.46	0.48	4.41	0.37	0.66	1093.18
D181	92.80	0.28	0.29	0.47	0.29	2.02	0.49	1.06	580.85
D182	79.04	0.12	0.28	0.27	0.30	3.94	0.50	0.74	616.92
D183	79.68	0.18	0.30	0.43	0.30	4.84	0.20	1.27	229.77
D184	80.80	0.19	0.23	0.37	0.43	4.21	0.23	1.47	209.49
D185	70.88	0.28	0.28	0.25	0.47	4.42	0.40	0.69	1023.59
D186	94.32	0.23	0.20	0.22	0.37	3.78	0.48	1.07	421.69

D187	80.56	0.33	0.20	0.36	0.32	2.40	0.34	0.95	775.53
D188	82.56	0.19	0.13	0.47	0.40	2.99	0.33	1.28	278.63
D189	87.28	0.18	0.32	0.35	0.39	2.59	0.28	1.47	220.55
D190	77.92	0.25	0.25	0.37	0.20	4.22	0.22	1.33	383.13
D191	65.28	0.24	0.27	0.30	0.50	4.99	0.38	0.60	1032.42
D192	66.48	0.24	0.33	0.39	0.47	4.39	0.47	0.52	1434.90
D193	76.88	0.12	0.16	0.26	0.40	2.75	0.38	1.00	300.76
D194	71.04	0.23	0.29	0.44	0.36	3.35	0.41	0.77	792.95
D195	65.52	0.34	0.24	0.31	0.27	3.19	0.23	0.67	1402.28
D196	77.28	0.33	0.29	0.41	0.28	4.74	0.30	0.94	879.28
D197	96.56	0.29	0.13	0.49	0.44	2.03	0.37	1.43	375.12
D198	73.36	0.26	0.10	0.45	0.31	2.19	0.38	0.85	689.93
D199	97.28	0.23	0.35	0.26	0.21	4.29	0.32	1.87	255.05
D200	66.88	0.32	0.28	0.34	0.45	4.21	0.41	0.60	1540.64
D201	97.04	0.21	0.30	0.21	0.36	2.21	0.34	1.89	215.14
D202	96.08	0.11	0.28	0.49	0.47	2.45	0.21	1.73	88.86
D203	86.40	0.21	0.13	0.44	0.42	2.84	0.27	1.66	212.23
D204	99.44	0.23	0.11	0.39	0.24	2.81	0.45	1.29	307.58
D205	66.08	0.23	0.17	0.27	0.41	4.12	0.24	0.88	536.11
D206	84.80	0.18	0.35	0.48	0.48	2.44	0.21	1.24	222.27
D207	94.72	0.22	0.35	0.24	0.28	4.06	0.28	1.87	232.62
D208	101.44	0.11	0.17	0.32	0.49	4.96	0.50	1.23	280.65
D209	104.40	0.14	0.16	0.32	0.49	4.50	0.28	2.27	79.53
D210	78.16	0.19	0.29	0.48	0.37	2.07	0.21	1.29	269.44
D211	99.92	0.14	0.35	0.21	0.45	2.39	0.40	1.45	209.63
D212	101.68	0.25	0.19	0.21	0.47	2.84	0.24	2.23	178.73
D213	102.72	0.31	0.12	0.37	0.30	4.40	0.21	1.66	280.59
D214	103.92	0.26	0.22	0.41	0.39	3.26	0.23	2.32	190.33
D215	81.20	0.13	0.22	0.28	0.23	2.14	0.43	1.02	361.86
D216	90.72	0.25	0.34	0.31	0.27	3.40	0.25	1.93	293.10
D217	101.92	0.28	0.16	0.48	0.29	4.27	0.24	1.91	227.80
D218	95.84	0.34	0.25	0.46	0.25	3.43	0.48	1.03	653.98
D219	94.00	0.15	0.29	0.41	0.21	4.43	0.25	1.80	119.61
D220	70.32	0.19	0.28	0.32	0.42	3.50	0.37	0.79	594.95
D221	85.60	0.32	0.15	0.26	0.26	2.24	0.41	0.98	653.90
D222	103.20	0.12	0.23	0.24	0.22	2.77	0.41	1.71	151.50
D223	70.48	0.12	0.20	0.44	0.33	2.21	0.38	0.83	400.60
D224	72.72	0.31	0.34	0.31	0.34	4.57	0.29	0.91	1004.50
D225	104.00	0.15	0.13	0.44	0.35	3.25	0.45	1.52	198.40

D226	98.88	0.17	0.27	0.49	0.43	3.92	0.32	1.70	160.64
D227	76.24	0.33	0.20	0.33	0.40	4.97	0.37	0.77	1019.60
D228	81.04	0.13	0.12	0.48	0.46	3.72	0.48	0.82	496.63
D229	98.08	0.22	0.11	0.25	0.41	3.13	0.50	1.14	370.21
D230	90.16	0.17	0.28	0.35	0.36	2.76	0.36	1.38	230.38
D231	103.84	0.25	0.18	0.24	0.30	2.48	0.43	1.50	263.11
D232	79.20	0.30	0.13	0.44	0.49	4.95	0.44	0.73	908.35
D233	99.36	0.16	0.32	0.24	0.27	3.47	0.41	1.49	219.70
D234	69.76	0.28	0.17	0.23	0.45	3.41	0.47	0.58	1222.87
D235	69.92	0.33	0.21	0.41	0.38	3.17	0.45	0.61	1495.14
D236	81.12	0.31	0.10	0.45	0.25	4.01	0.34	0.93	678.40
D237	89.52	0.12	0.17	0.29	0.41	2.54	0.27	1.79	97.69
D238	93.68	0.31	0.21	0.48	0.48	4.13	0.42	1.10	554.04
D239	71.68	0.11	0.22	0.44	0.44	2.74	0.36	0.85	361.85
D240	93.04	0.16	0.28	0.26	0.45	2.65	0.36	1.50	199.34
D241	81.52	0.14	0.26	0.43	0.47	3.58	0.46	0.86	482.79
D242	99.84	0.28	0.32	0.49	0.44	4.26	0.32	1.89	326.18
D243	94.40	0.30	0.32	0.43	0.39	2.65	0.38	1.38	479.08
D244	96.96	0.31	0.24	0.49	0.20	3.16	0.42	1.24	478.66

References

[1] A. R. Smith, S. Gwo, and C. K. Shih, "A new high-resolution two-dimensional micropositioning device for scanning probe microscopy applications," *Rev. Sci. Instrum.*, vol. 65, no. 10, pp. 3216–3219, Oct. 1994.

[2] B. J. Kenton and K. K. Leang, "Design and Control of a Three-Axis Serial-Kinematic High-Bandwidth Nanopositioner," *IEEEASME Trans. Mechatron.*, vol. 17, no. 2, pp. 356–369, Apr. 2012.

[3] G. Schitter, K. J. Astrom, B. E. DeMartini, P. J. Thurner, K. L. Turner, and P. K. Hansma, "Design and Modeling of a High-Speed AFM-Scanner," *IEEE Trans. Control Syst. Technol.*, vol. 15, no. 5, pp. 906–915, Sep. 2007.

[4] Y. K. Yong, S. O. R. Moheimani, B. J. Kenton, and K. K. Leang, "Invited Review Article: High-speed flexure-guided nanopositioning: Mechanical design and control issues," *Rev. Sci. Instrum.*, vol. 83, no. 12, p. 121101, Dec. 2012.

[5] C.-W. Lee and S.-W. Kim, "An ultraprecision stage for alignment of wafers in advanced microlithography," *Precis. Eng.*, vol. 21, no. 2–3, pp. 113–122, Sep. 1997.

[6] K. Sugihara, I. Mori, T. Tojo, C. Ito, M. Tabata, and T. Shinozaki, "Piezoelectrically driven $X\,Y\,\theta$ table for submicron lithography systems," *Rev. Sci. Instrum.*, vol. 60, no. 9, pp. 3024–3029, Sep. 1989.

[7] P. Vettiger, M. Despont, U. Drechsler, U. Durig, and et al, "The 'millipede'--more than one thousand tips for future AFM data storage," *IBM J. Res. Dev. Armonk*, vol. 44, no. 3, pp. 323–340, May 2000.

[8] N. K. Roy, C. S. Foong, and M. A. Cullinan, "Design of a Micro-Scale Selective Laser Sintering System," p. 14.

[9] Z. Zhang, P. Yan, and G. Hao, "A Large Range Flexure-Based Servo System Supporting Precision Additive Manufacturing," *Engineering*, vol. 3, no. 5, pp. 708–715, Oct. 2017.

[10] S. Gonda, T. Kurosawa, and Y. Tanimura, "Mechanical performances of a symmetrical, monolithic three-dimensional fine-motion stage for nanometrology," *Meas. Sci. Technol.*, vol. 10, no. 11, pp. 986–993, Nov. 1999.

[11] M. L. Culpepper and G. Anderson, "Design of a low-cost nano-manipulator which utilizes a monolithic, spatial compliant mechanism," *Precis. Eng.*, vol. 28, no. 4, pp. 469–482, Oct. 2004.

[12] Yuen Kuan Yong, S. S. Aphale, and S. O. Reza Moheimani, "Design, Identification, and Control of a Flexure-Based *XY* Stage for Fast Nanoscale Positioning," *IEEE Trans. Nanotechnol.*, vol. 8, no. 1, pp. 46–54, Jan. 2009.

[13] L.-J. Lai, G.-Y. Gu, and L.-M. Zhu, “Design and control of a decoupled two degree of freedom translational parallel micro-positioning stage,” *Rev. Sci. Instrum.*, vol. 83, no. 4, p. 045105, Apr. 2012.

[14] K.-B. Choi and D.-H. Kim, “Monolithic parallel linear compliant mechanism for two axes ultraprecision linear motion,” *Rev. Sci. Instrum.*, vol. 77, no. 6, p. 065106, Jun. 2006.

[15] S. Devasia, E. Eleftheriou, and S. O. R. Moheimani, “A Survey of Control Issues in Nanopositioning,” *IEEE Trans. Control Syst. Technol.*, vol. 15, no. 5, pp. 802–823, Sep. 2007.

[16] G. Dai, F. Pohlenz, H.-U. Danzebrink, M. Xu, K. Hasche, and G. Wilkening, “Metrological large range scanning probe microscope,” *Rev. Sci. Instrum.*, vol. 75, no. 4, pp. 962–969, Apr. 2004.

[17] A. Sinno *et al.*, “Enlarged atomic force microscopy scanning scope: Novel sample-holder device with millimeter range,” *Rev. Sci. Instrum.*, vol. 78, no. 9, p. 095107, Sep. 2007.

[18] H. Liu, B. Lu, Y. Ding, Y. Tang, and D. Li, “A motor-piezo actuator for nano-scale positioning based on dual servo loop and nonlinearity compensation,” *J. Micromechanics Microengineering*, vol. 13, no. 2, pp. 295–299, Mar. 2003.

[19] J. A. Kramar, “Nanometre resolution metrology with the Molecular Measuring Machine,” *Meas. Sci. Technol.*, vol. 16, no. 11, pp. 2121–2128, Nov. 2005.

[20] S. Awtar and G. Parmar, “DESIGN OF A LARGE RANGE XY NANOPOSITIONING SYSTEM,” p. 13.

[21] Tien-Tung Chung, Chih-Hsiang Chu, K.-C. Fan, Jia-Yush Yen, and Kou-I Szu, “Development of a nano-positioning planar motion stage,” in *2010 2nd International Conference on Mechanical and Electronics Engineering*, Kyoto, Japan, 2010, pp. V1-122-V1-126.

[22] T. Tsumura, H. Yoshioka, H. Shinno, and H. Sawano, “Magnetically preloaded aerostatic guideway for high speed nanometer positioning,” *J. Adv. Mech. Des. Syst. Manuf.*, vol. 8, no. 4, pp. JAMDSM0054–JAMDSM0054, 2014.

[23] W. Kim, S. Verma, and H. Shakir, “Design and precision construction of novel magnetic-levitation-based multi-axis nanoscale positioning systems,” *Precis. Eng.*, vol. 31, no. 4, pp. 337–350, Oct. 2007.

[24] M. Holmes, R. Hocken, and D. Trumper, “The long-range scanning stage: a novel platform for scanned-probe microscopy,” *Precis. Eng.*, vol. 24, no. 3, pp. 191–209, Jul. 2000.

[25] S. Awtar, “Synthesis and Analysis of Parallel Kinematic XY Flexure Mechanisms,” p. 198.

[26] Q. Xu, “Design and Development of a Compact Flexure-Based XY Precision Positioning System With Centimeter Range,” *IEEE Trans. Ind. Electron.*, vol. 61, no. 2, pp. 893–903, Feb. 2014.

[27] X. Zhou, H. Xu, J. Cheng, N. Zhao, and S.-C. Chen, “Flexure-based Roll-to-roll Platform: A Practical Solution for Realizing Large-area Microcontact Printing,” *Sci. Rep.*, vol. 5, no. 1, p. 10402, Sep. 2015.

[28] R. M. Panas and J. B. Hopkins, “Eliminating Underconstraint in Double Parallelogram Flexure Mechanisms,” *J. Mech. Des.*, vol. 137, no. 9, p. 092301, Jul. 2015.

[29] H. Liu, S. Fan, X. Xie, Z. Zhang, and D. Fan, “Design and modeling of a novel monolithic parallel XY stage with centimeters travel range,” *Adv. Mech. Eng.*, vol. 9, no. 11, p. 168781401772962, Nov. 2017.

[30] Z. Wu and Q. Xu, “Design, optimization and testing of a compact XY parallel nanopositioning stage with stacked structure,” *Mech. Mach. Theory*, vol. 126, pp. 171–188, Aug. 2018.

[31] S. Awtar and A. H. Slocum, “Constraint-Based Design of Parallel Kinematic XY Flexure Mechanisms,” *J. Mech. Des.*, vol. 129, no. 8, p. 816, 2007.

[32] Q. Xu, “New Flexure Parallel-Kinematic Micropositioning System With Large Workspace,” *IEEE Trans. Robot.*, vol. 28, no. 2, pp. 478–491, Apr. 2012.

[33] Q. Xu, “A modular two-axis compliant parallel micropositioning stage with long travel range,” in *2013 IEEE International Conference on Information and Automation (ICIA)*, Yinchuan, China, 2013, pp. 898–903.

[34] S. Wan and Q. Xu, “Design and analysis of a new compliant XY micropositioning stage based on Roberts mechanism,” *Mech. Mach. Theory*, vol. 95, pp. 125–139, Jan. 2016.

[35] N. K. Roy and M. A. Cullinan, “Design and characterization of a two-axis, flexure-based nanopositioning stage with 50 mm travel and reduced higher order modes,” *Precis. Eng.*, vol. 53, pp. 236–247, Jul. 2018.

[36] J. W. Ryu, D.-G. Gweon, and K. S. Moon, “Optimal design of a flexure hinge based XYφ wafer stage,” *Precis. Eng.*, vol. 21, no. 1, pp. 18–28, Jul. 1997.

[37] M. P. Dang, T.-P. Dao, and H. Giang Le, “Optimal Design of a New Compliant XY Micro positioning Stage for Nanoindentation Tester Using Efficient Approach of Taguchi Method, Response Surface Method and NSGA-II,” in *2018 4th International Conference on Green Technology and Sustainable Development (GTSD)*, Ho Chi Minh City, 2018, pp. 1–6.

[38] S.-C. Huang and T.-P. Dao, “Design and computational optimization of a flexure-based XY positioning platform using FEA-based response surface methodology,” *Int. J. Precis. Eng. Manuf.*, vol. 17, no. 8, pp. 1035–1048, Aug. 2016.

[39] Y. Qin, B. Shirinzadeh, Y. Tian, D. Zhang, and U. Bhagat, "Design and Computational Optimization of a Decoupled 2-DOF Monolithic Mechanism," *IEEEASME Trans. Mechatron.*, vol. 19, no. 3, pp. 872–881, Jun. 2014.

[40] H.-H. Pham and I.-M. Chen, "Stiffness modeling of flexure parallel mechanism," *Precis. Eng.*, vol. 29, no. 4, pp. 467–478, Oct. 2005.

[41] N. Lobontiu, "Compliance-based matrix method for modeling the quasi-static response of planar serial flexure-hinge mechanisms," *Precis. Eng.*, vol. 38, no. 3, pp. 639–650, Jul. 2014.

[42] M. Verotti, "Effect of initial curvature in uniform flexures on position accuracy," *Mech. Mach. Theory*, vol. 119, pp. 106–118, Jan. 2018.

[43] N. Li, H.-J. Su, and X.-P. Zhang, "Accuracy Assessment of Pseudo-Rigid-Body Model for Dynamic Analysis of Compliant Mechanisms," *J. Mech. Robot.*, vol. 9, no. 5, p. 054503, Aug. 2017.

[44] V. K. Venkiteswaran and H.-J. Su, "A Versatile 3R Pseudo-Rigid-Body Model for Initially Curved and Straight Compliant Beams of Uniform Cross Section," *J. Mech. Des.*, vol. 140, no. 9, p. 092305, Jul. 2018.

[45] S. Xiao, Y. Li, and X. Zhao, "Design and analysis of a novel flexure-based XY micro-positioning stage driven by electromagnetic actuators," in *Proceedings of 2011 International Conference on Fluid Power and Mechatronics*, 2011, pp. 953–958.

[46] Y. Li and Q. Xu, "A Totally Decoupled Piezo-Driven XYZ Flexure Parallel Micropositioning Stage for Micro/Nanomanipulation," *IEEE Trans. Autom. Sci. Eng.*, vol. 8, no. 2, pp. 265–279, Apr. 2011.

[47] Y. Jiang, T.-M. Li, and L.-P. Wang, "Stiffness modeling of compliant parallel mechanisms and applications in the performance analysis of a decoupled parallel compliant stage," *Rev. Sci. Instrum.*, vol. 86, no. 9, p. 095109, Sep. 2015.

[48] B. Zettl, W. Szyszkowski, and W. J. Zhang, "On Systematic Errors of Two-Dimensional Finite Element Modeling of Right Circular Planar Flexure Hinges," *J. Mech. Des.*, vol. 127, no. 4, p. 782, 2005.

[49] T. W. Simpson, J. D. Poplinski, P. N. Koch, and J. K. Allen, "Metamodels for Computer-based Engineering Design: Survey and recommendations," *Eng. Comput.*, vol. 17, no. 2, pp. 129–150, Jul. 2001.

[50] D. Lechevalier, S. Hudak, R. Ak, Y. T. Lee, and S. Foufou, "A neural network meta-model and its application for manufacturing," in *2015 IEEE International Conference on Big Data (Big Data)*, Santa Clara, CA, USA, 2015, pp. 1428–1435.